Faraday Discussions

Cite this: *Faraday Discuss.*, 2026, **264**, 439

PAPER

Processing-driven chemical ordering and its effect on magnetic properties in a high entropy alloy

V. Chaudhary, *[a] S. Dasari,[b] A. Sharma,[c] R. V. Ramanujan [d] and R. Banerjee[c]

Received 30th June 2025, Accepted 24th July 2025
DOI: 10.1039/d5fd00105f

The influence of chemical ordering and its length scale on the magnetic behaviour of the $Al_{0.2}Ti_{0.3}Co_{1.5}CrFeNi_{1.5}$ high entropy alloy (HEA) was investigated across three distinct microstructural conditions, including a solution annealed state, an annealed condition at 750 °C, and a cold rolled plus annealed condition. These processing routes produced changes in the volume fraction, size, and morphology of $L1_2$ ordered precipitates along with the formation of a minor $L2_1$ phase in the annealed states. Magnetic measurements performed between 2 K and 300 K revealed clear differences in saturation magnetization, coercivity, and magnetic transition temperatures across the three conditions. The solution annealed condition exhibited a single magnetic transition near 48 K and low coercivity, consistent with a fine dispersion of coherent $L1_2$ precipitates. In the annealed and cold rolled conditions, coarsening and morphological evolution of the $L1_2$ phase led to the emergence of a second magnetic transition at lower temperatures, attributed to partial magnetic decoupling of the precipitates. Coercivity increased significantly in these conditions due to enhanced domain wall pinning, while residual hysteresis at 300 K is attributed to a combination of minor $L2_1$ phase at grain boundaries and microstructural features in the cold-worked condition. These results demonstrate that chemical ordering and its structural evolution play a central role in governing low temperature magnetic behaviour in this alloy system. The findings contribute to the broader understanding of multifunctional HEAs that combine tunable magnetic properties with excellent mechanical performance.

[a]*Industrial and Materials Science, Chalmers University of Technology, Gothenburg, SE-41296, Sweden. E-mail: varunc@chalmers.se*
[b]*Metallurgical, Materials and Biomedical Engineering Department, University of Texas at El Paso, El Paso, TX, 79968, USA*
[c]*Department of Materials Science and Engineering, University of North Texas, Denton, TX, 76207, USA*
[d]*School of Materials Science and Engineering, Nanyang Technological University, 639798, Singapore*

1. Introduction

High entropy alloys (HEA), composed of multiple principal elements in near equiatomic proportions, have gained attention for their promising structural and functional properties.[1–5] Among these, FCC-based CoCrFeNi-derived alloys are particularly attractive due to their good thermal stability, corrosion resistance, and mechanical strength.[6,7] Alloying with Al and Ti has been shown to promote chemical ordering, leading to the formation of $L1_2$ type precipitates, which improve strength by precipitation hardening. In some cases, minor amounts of ordered intermetallic phases such as $L2_1$ Heusler-like structures can also form, particularly at grain boundaries. While mechanical properties of such precipitation strengthened HEA have been well studied,[7] their magnetic behavior, especially how it evolves with phase formation and ordering length scale, has been rarely explored. This is important because magnetic properties in these systems are closely tied to composition, atomic scale ordering, and microstructure. The presence of ordered phases such as $L1_2$ and $L2_1$, and their interaction with the FCC matrix, can significantly affect magnetization, coercivity, and magnetic transition temperatures.

Nanoscale phase engineering in high-entropy alloys and compositionally complex alloys enables the simultaneous optimization of magnetic and mechanical performance.[8–13] For example, a Fe–CoNi–Ta–Al alloy with coherent nanoprecipitates uniformly dispersed in an FCC matrix exhibited enhanced ultimate tensile strength ($\approx$1526 MPa) and good ductility ($\sim$15%), while maintaining a coercivity close to 10 Oe.[11] In a related system, the $Fe_{32.6}Co_{27.7}Ni_{27.7}Ta_5Al_7$ HEA exhibited a dual-phase microstructure containing $L1_2$ precipitates within a ferromagnetic FCC matrix. By tailoring the precipitate size, this alloy achieved a low coercivity ($\sim$1 Oe), moderate saturation magnetization ($\sim$100 emu g^{-1}), and high ductility ($\sim$54% elongation).[12] These properties resulted from the combined effects of precipitation strengthening, solid–solution hardening, and microband refinement, with minimal magnetic pinning due to the full coherence and uniform distribution of the precipitates. Advanced electron microscopy reveals that magnetization reversal in $Al_{0.3}CoFeNi$ evolves from a nucleation-controlled mechanism in the FCC + $L1_2$ state (domain wall width $\sim$171 nm) to a pinning-dominated process in a nanorod-containing BCC/B2 matrix, where the domain wall width narrows to $\sim$35 nm.[9]

Magnetic materials are key components in everyday life,[14,15] and they are not only important for room temperature or elevated temperature applications but are also increasingly relevant in the low temperature range.[5,16] In the 20 to 80 K range, they are being explored for magnetic refrigeration, particularly in pre-cooling stages for hydrogen liquefaction, as well as in cryogenic actuators and control systems where both mechanical reliability and magnetic responsiveness are required. At lower temperatures, around 2 to 10 K, such materials are used in superconducting magnet systems, magnetic shielding, and low temperature sensing, including emerging quantum devices and precision instrumentation.[17,18] In these settings, materials with well-defined magnetic transitions, stable coercivity, and reliable microstructural stability are essential for functional integration and performance.

In this context, the $Al_{0.2}Ti_{0.3}Co_{1.5}CrFeNi_{1.5}$ HEA is a valuable model system for studying the relationship between chemical ordering and magnetic behavior.

Although it is not designed to exhibit strong ferromagnetism at room temperature, it develops multiple ordered phases including $L1_2$ precipitates of different morphology and size scale and, in some conditions, a minor $L2_1$ phase. The size, volume fraction, and morphology of these phases can be tuned through thermal and thermomechanical processing. These features enable a systematic investigation of how ordering at different length scales influences saturation magnetization, coercivity, and the emergence of distinct magnetic transitions. The insights gained from this system are relevant for the broader design of multiphase alloys with balanced magnetic and mechanical performance in low temperature environments.

2. Experimental methods

The $Al_{0.2}Ti_{0.3}Co_{1.5}CrFeNi_{1.5}$ alloy was synthesized by arc melting a mixture of elemental metals under an argon atmosphere. To ensure compositional homogeneity, the alloy was re-melted multiple times. The ingot was then homogenized at 1150 °C for 6 hours and water quenched to room temperature. Four processing conditions were investigated. The solution-annealed (SA) condition corresponds to the homogenized and quenched state. In the second condition (SA750), the SA sample was annealed at 750 °C for 50 hours. The third and fourth conditions (60CRA and 90CRA) involved cold rolling the SA material to 60% and 90% thickness reductions, respectively, followed by annealing at 750 °C for 50 hours. All heat treatments were performed in sealed quartz tubes under argon and were subsequently quenched in water.

Microstructural characterization was carried out using scanning electron microscopy (SEM) equipped with energy-dispersive X-ray spectroscopy (EDS) and electron backscatter diffraction (EBSD), as well as transmission electron microscopy (TEM). Site-specific TEM lamellae were prepared using focused ion beam (FIB) lift-out techniques. Atom probe tomography (APT) was performed in laser mode to analyse nanoscale chemical partitioning.

Magnetic measurements were carried out using a Physical Property Measurement System (PPMS EverCool, Quantum Design, USA). Temperature-dependent magnetization was measured under zero-field-cooled (ZFC) and field-cooled (FC) conditions with an applied magnetic field of 1000 Oe, over the temperature range of 5 K to 400 K. Isothermal magnetization (M–H) curves were recorded at 2 K, 10 K, 50 K, 100 K, and 300 K using applied magnetic fields of $\pm$5000 Oe. The term "saturation magnetization" (M_s) in this study refers to the magnetization measured at an applied field of 5000 Oe. This may not correspond to true saturation under conditions above the magnetic transition temperature, where the material is paramagnetic or exhibits a mixed ferromagnetic and paramagnetic response. Nevertheless, it is used as a comparative measure of magnetic behaviour across different conditions.

3. Results and discussion

3.1. Thermodynamic modelling

The alloy composition was selected to enable the precipitation of nanoscale $L1_2$ in an FCC matrix, thereby enhancing its strength. Solution thermodynamic modelling in Fig. 1(a) shows an isopleth constructed by varying the Al/Ti ratio in

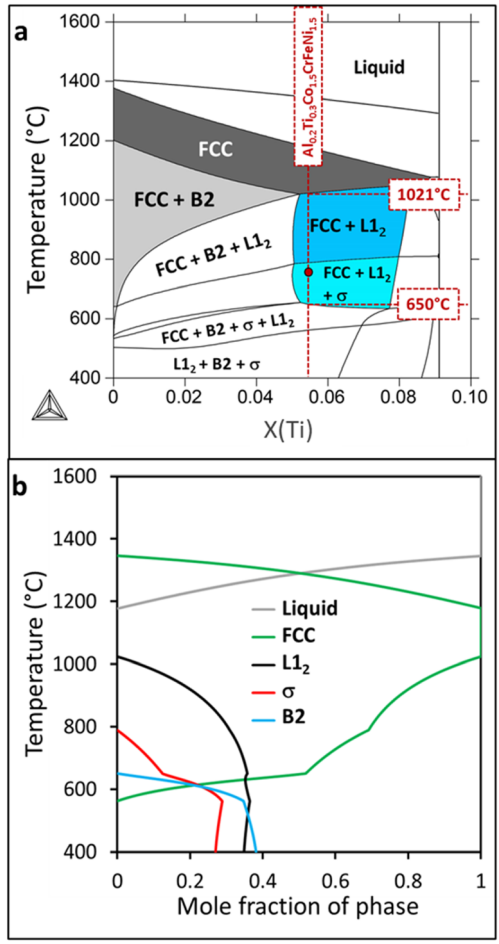

Fig. 1 (a) Pseudo-binary isopleth for $Al_{0.5-x}Ti_xCo_{1.5}CrFeNi_{1.5}$ ($x = 0$ to 0.5 in relative mole fraction). (b) Phase fraction *vs.* temperature diagram for $Al_{0.2}Ti_{0.3}Co_{1.5}CrFeNi_{1.5}$.

$Al_{0.5-x}Ti_xCo_{1.5}CrFeNi_{1.5}$ alloy. The current alloy $Al_{0.2}Ti_{0.3}Co_{1.5}CrFeNi_{1.5}$, as indicated by the red dashed line in this figure, exhibits a large FCC + $L1_2$ phase field. The phase fraction *vs.* temperature plot in Fig. 1(b) shows that ~35% $L1_2$ can be precipitated at 750 °C.

3.2. Microstructural characterization

The microstructural characterization results from SA and SA750 conditions are shown in Fig. 2. The SEM backscattered images in Fig. 2(a and b) show the coarse-grain microstructures of SA and SA750 conditions, respectively. They are expected to be single-phase FCC, as predicted by the thermodynamic modelling in Fig. 1. The inset in Fig. 2(b) shows a high-magnification image of the precipitates in the SA750 condition. This microstructure, likely consisting of $L1_2$ nanoprecipitates in an FCC matrix, is also consistent with the prediction (Fig. 1).

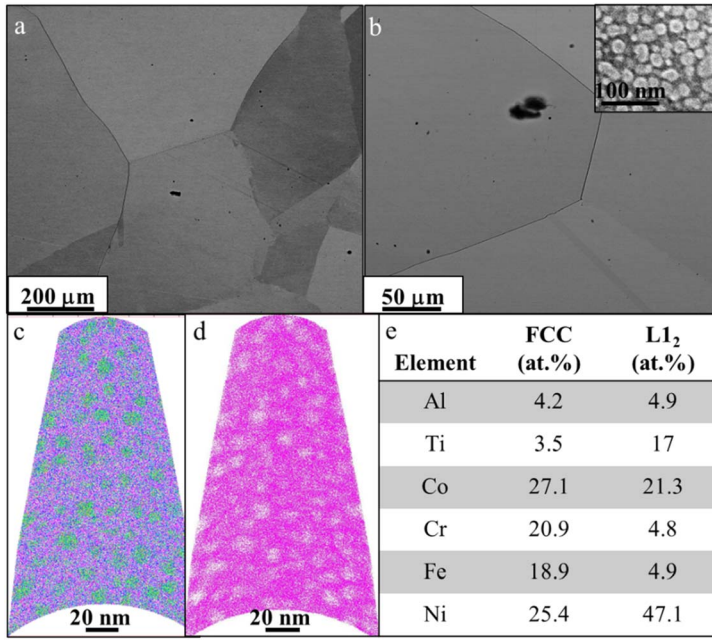

e

Element	FCC (at.%)	$L1_2$ (at.%)
Al	4.2	4.9
Ti	3.5	17
Co	27.1	21.3
Cr	20.9	4.8
Fe	18.9	4.9
Ni	25.4	47.1

Fig. 2 Backscattered SEM images of (a) SA and (b) SA750 conditions. The inset in (b) shows a high magnification image of the precipitates in the SA750 condition. APT results from the SA condition are shown in (c–e). (c) A 2D section of the superimposition of all raw ion maps (Al = blue, Ti = dark green, Co = blue, Cr = light pink, Fe = dark pink, Ni = green), (d) Fe raw ion map section, (e) FCC and $L1_2$ compositions in the SA condition.

APT analysis confirms the presence of nanoscale $L1_2$ precipitates in both SA and SA750 conditions. Representative APT reconstructions from the SA condition are shown in Fig. 2(c and d). The superimposed ion map in Fig. 2(c) highlights a uniform distribution of ~5 nm spherical precipitates with an estimated volume fraction of ~9%, which appear as Ni-rich and Fe-depleted features in the Fe ion map in Fig. 2(d). Compositional partitioning between matrix and precipitate phases is summarized in the table given in Fig. 2(e), showing Ti and Al enrichment in the $L1_2$ phase. While the APT data correspond to the SA condition, prior characterization[7] indicates that in SA750, the $L1_2$ precipitates coarsen to ~25 nm and grow in volume fraction to ~46%.

Fig. 3(a and b) show the microstructures of 60CRA and 90CRA conditions respectively. Partial recrystallization can be observed in the 60CRA condition as indicated by the red boundary between recrystallized and non-recrystallized regions in Fig. 3(a). On the other hand, a fully recrystallized fine-grained structure is visible in the 90CRA condition in Fig. 3(b). Additionally, dark polygonal or dot-like precipitates are visible in both 60CRA and 90CRA conditions. The degree of recrystallization in the two conditions was further studied using EBSD. Fig. 3(c) shows the inverse pole figure (IPF) map from the 60CRA condition. Here, coarse non-recrystallized grains, as indicated by the orientation contrast, *i.e.*, variations in color within the same grain, and fine recrystallized grains, can be seen to coexist. Islands of recrystallized grains can also be observed in non-recrystallized grains, which result from higher strain in those regions. The IPF map from the

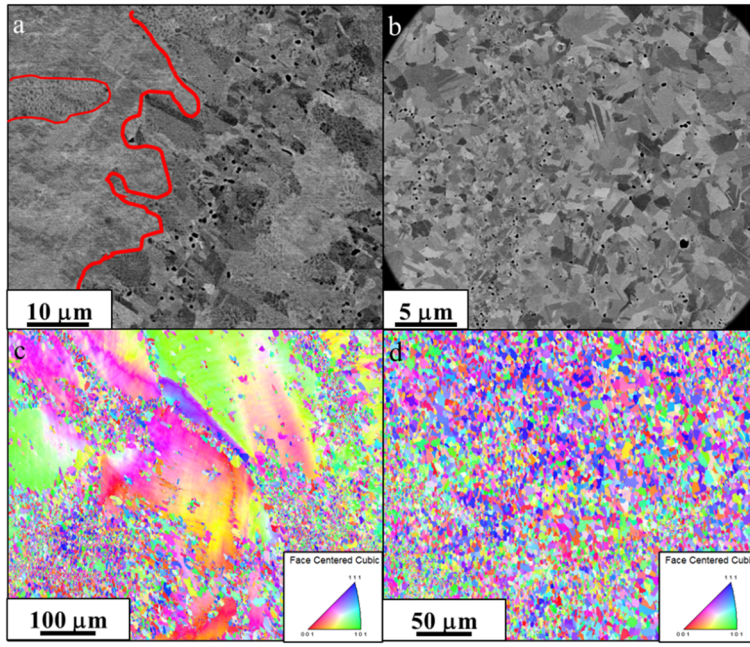

Fig. 3 Backscattered SEM images of (a) 60CRA and (b) 90CRA conditions. EBSD IPF maps show (c) a partially recrystallized microstructure in 60CRA and (d) a fully recrystallized microstructure in 90CRA.

90CRA condition in Fig. 3(d) shows a homogeneously recrystallized grain structure.

The nanoscale microstructures in 60CRA and 90CRA conditions were investigated using TEM to reveal $L1_2$ precipitation, as expected from annealing at 750 °C (refer to Fig. 1). While detailed microstructural characterization of all conditions was reported elsewhere,[7] two important TEM results are shown in Fig. 4. The TEM results from a non-recrystallized region in the 60CRA condition are shown in Fig. 4(a–c). The HAADF-STEM image in Fig. 4(a) and the Ti and Ni STEM-EDS maps in Fig. 4(b and c) show blocky $L1_2$ precipitates within this region. On the other hand, the recrystallized grains in 90CRA conditions show a rod-like or lamellar $L1_2$ precipitation in Fig. 4(d–f).

The lamellar morphology is much clearer from the APT results from the 90CRA condition shown in Fig. 5. Fig. 5(a–c) show 2D sections of maps with all ions, Ti, and Fe, respectively. The compositions of the $L1_2$ and FCC phases are also listed in the table in Fig. 5(d). The two precipitate morphologies, *i.e.*, spherical or blocky and lamellar, arise from two distinct transformation pathways: continuous precipitation and discontinuous precipitation. In the case of SA750 and the non-recrystallized regions of the 60CRA condition, $L1_2$ precipitates nucleate homogeneously within the grains and coarsen with annealing time. This leads to spherical or blocky precipitates, as seen in Fig. 4(b and c). However, when there is a driving force for recrystallization, the precipitation occurs concurrently with grain boundary migration leading to rod-like $L1_2$ precipitation. This reaction,

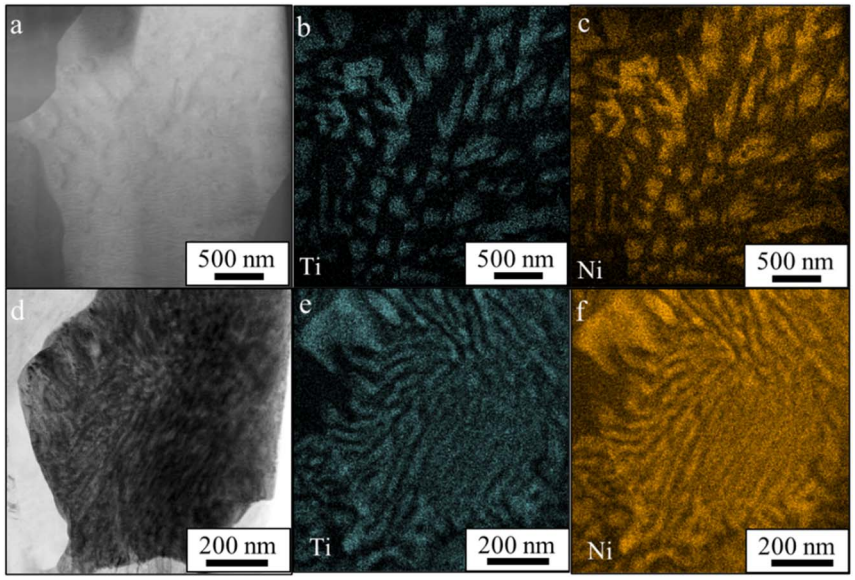

Fig. 4 (a) HAADF-STEM image and (b) Ti and (c) Ni STEM-EDS maps from a non-recrystallized grain in the 60CRA condition show blocky $L1_2$ precipitation. (d) HAADF-STEM image and (e) Ti and (f) Ni STEM-EDS maps from a recrystallized grain in the 90CRA condition show rod-like $L1_2$ precipitation.

known as discontinuous precipitation,[19,20] occurs in the recrystallized regions of 60CRA and 90CRA conditions.

The summary of the microstructures of the four processing conditions is as follows. The SA condition has a coarse grain structure with ~5 nm diameter $L1_2$ precipitates. These non-equilibrium precipitates formed during water quenching, as reported in similar alloys previously.[21] SA750 also exhibited a coarse grain structure but with a uniform distribution of equilibrium $L1_2$ precipitates. The average precipitate diameter in SA750 is 25 nm. The 60CRA condition exhibited a partially recrystallized microstructure. The non-recrystallized grains contained blocky $L1_2$ precipitates (formed *via* continuous precipitation) while the recrystallized grains contained rod-like $L1_2$ precipitates (formed *via* discontinuous precipitation). 90CRA condition has a fully recrystallized grain structure with rod-like $L1_2$ precipitates. The approximate length and diameter of nano-rod $L1_2$ precipitates in the 90CRA condition are ~330 nm and ~30 nm, respectively. It is worth noting that the length may span up to the grain size (1.8 microns in 90CRA), but it is usually smaller due to processes such as branching and coarsening. A minor fraction of $L2_1$ precipitates also exists in both 60CRA and 90CRA conditions, which appear as dark polygonal or dot-like precipitates in Fig. 3.

3.3. Magnetic properties

Four distinct microstructural conditions, SA, SA750, 60CRA, and 90CRA, achieved *via* four distinct thermo-mechanical processing routes, have been discussed in the previous section. Since the SA, SA750, and 90CRA conditions exhibited a nominally homogeneous microstructure, while the 60CRA condition revealed

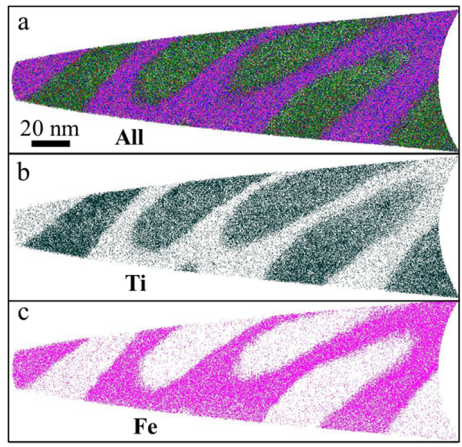

d

Element	FCC (at.%)	$L1_2$ (at.%)
Al	2.2	7.1
Ti	0.9	16.7
Co	31.8	15.8
Cr	25.6	2.1
Fe	23.4	2.4
Ni	16.1	55.9

Fig. 5 APT results from the 90CRA condition. (a) A 2D section of the superimposition of all raw ion maps (Al = blue, Ti = dark green, Co = blue, Cr = light pink, Fe = dark pink, Ni = green), (b) Ti raw ion map section, (c) Fe raw ion map section, and (d) FCC and $L1_2$ compositions in the 90CRA condition.

a partially recrystallized inhomogeneous condition, this condition was not analysed further in terms of magnetic properties. The following section describes the magnetic behaviour of the SA, SA750, and 90CRA conditions.

3.3.1. Magnetic behaviour of the SA condition. The SA condition, consisting of a fully FCC matrix with a fine dispersion of $L1_2$ precipitates (~5 nm, ~9% volume fraction), shows a clear temperature dependence in both saturation magnetization (M_s) and coercivity (H_c) (Fig. 6a and b). M_s decreases gradually from 27.7 emu g^{-1} at 2 K to 26.9 emu g^{-1} at 10 K, 17.5 emu g^{-1} at 50 K, and 5.4 emu g^{-1} at 100 K, reflecting the loss of long-range magnetic order as the system approaches and exceeds its Curie temperature (T_c) (Fig. 6b). H_c increases from 1.6 Oe at 2 K to 4.8 Oe at 10 K, reaching a maximum of 8.5 Oe around 48 K, and then slightly decreases to 8.2 Oe at 100 K (Fig. 6b). The relatively high coercivity near the T_c is attributed to the increase in magnetic anisotropy and exchange stiffness, which enhances resistance to domain wall motion as the system approaches magnetic ordering. Similar behaviour has been reported in nanocrystalline soft magnetic alloys, where exchange-decoupled grains lead to independent switching and domain wall formation near the decoupling temperature.[22]

The M–T curve, measured under zero-field-cooled and field-cooled protocols with a 1000 Oe applied field (Fig. 6c), reveals a single magnetic transition near 48 K, as indicated by the minimum in the dM/dT curve (Fig. 6d).

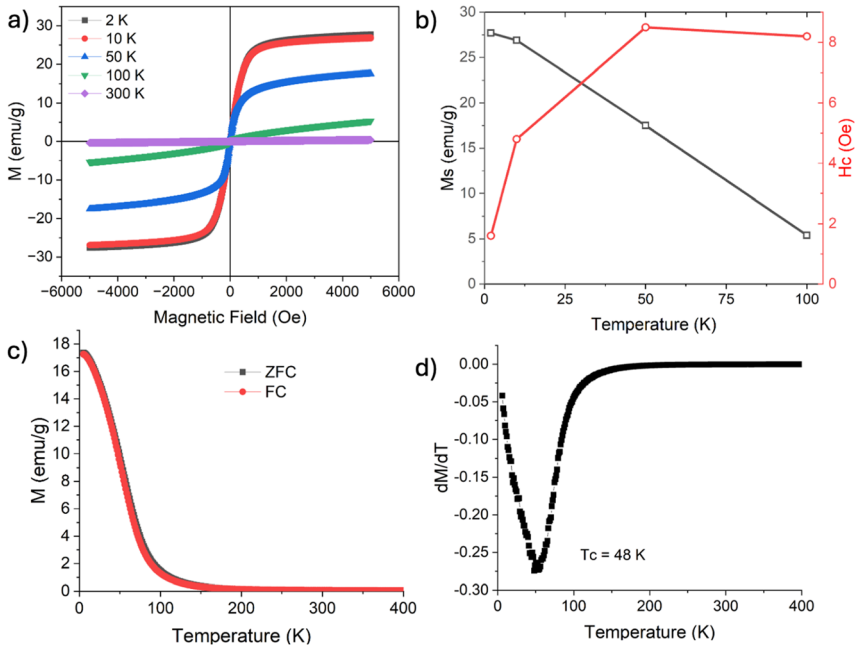

Fig. 6 Magnetic behaviour of the solution-annealed (SA) condition. (a) Isothermal magnetization (M–H) loops measured at multiple temperatures, showing ferromagnetic behaviour at low temperature and a paramagnetic behaviour at room temperature. (b) Temperature dependence of saturation magnetization (M_s, left axis, black squares) and coercivity (H_c, right axis, red circles). (c) Zero-field-cooled (ZFC) and field-cooled (FC) magnetization curves measured in a 1000 Oe applied field, revealing a single magnetic transition. (d) Derivative of magnetization (dM/dT) used to determine the Curie temperature, $T_c \approx 48$ K.

3.3.2. Magnetic behaviour of the SA750 condition. The SA750 condition, obtained by homogenization at 1150 °C followed by annealing at 750 °C for 50 hours, reflects the influence of a multiphase microstructure on magnetic response. M_s decreases with increasing temperature, from 17.1 emu g^{-1} at 2 K to 16.5 at 10 K, 10.1 at 50 K, and 3.7 at 100 K (Fig. 7a and b). These values are lower than those of the SA condition, likely due to Ni depletion and Cr enrichment in the FCC matrix after partitioning into $L1_2$. H_c is highest at 2 K (19.1 Oe), decreasing to 10.7 Oe at 10 K and reaching a minimum of 4.4 Oe at 50 K, before rising to 7.6 Oe at 100 K (Fig. 7b). This coercivity trend differs from the SA condition and reflects stronger domain wall pinning at low temperatures due to coarser and higher-volume-fraction $L1_2$ precipitates (~25 nm, ~46%). The minimum in H_c occurs between the T_c of the $L1_2$ phase (~36 K) and the FCC matrix (~90 K), and is attributed to thermally assisted depinning as magnetic stiffness and interphase coupling are progressively weakened with increasing temperature.

The M–T curve recorded under ZFC and FC protocols in an applied field of 1000 Oe shows two magnetic transitions (Fig. 7c). The higher T_c (90 K), identified from the dM/dT curve (Fig. 7d), corresponds to the FCC matrix, which becomes enriched in Fe and Co due to Ni, Al and Ti partitioning into the $L1_2$ phase. The

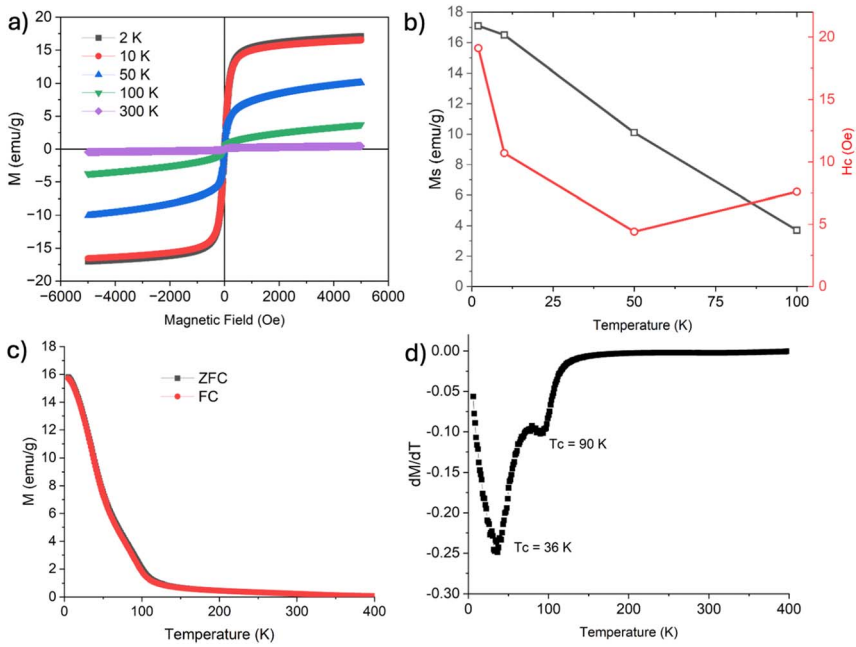

Fig. 7 Magnetic behaviour of the SA750 condition. (a) M–H loops measured at different temperatures, showing ferromagnetic behaviour at low temperatures with decreasing magnetization at higher temperatures. (b) Temperature dependence of saturation magnetization (M_s, left axis, black squares) and coercivity (H_c, right axis, red circles). (c) ZFC and FC magnetization curves recorded under a 1000 Oe applied field, showing a gradual decrease in magnetization with increasing temperature. (d) First derivative of magnetization (dM/dT), indicating two distinct magnetic transitions with Curie temperatures (T_c) at ~36 K and ~90 K.

lower transition at ~36 K likely arises from magnetic ordering within the $L1_2$ precipitates, which become partially decoupled from the matrix as their size and volume increase. Their composition, enriched in Al and Ti but still containing ferromagnetic Ni and Co, supports localized magnetic ordering distinct from the matrix.

3.3.3. Magnetic behaviour of the 90CRA condition. The 90CRA condition, produced by 90% cold rolling followed by annealing at 750 °C for 50 hours, exhibits a distinct magnetic response governed by its fine-grained, recrystallized microstructure and discontinuous precipitation of the $L1_2$ phase. The saturation magnetization decreases with increasing temperature, from 14.9 emu g^{-1} at 2 K to 12.3 at 10 K, 8.3 at 50 K, and 3.1 at 100 K (Fig. 8a and b). These values are lower than those observed in SA and SA750, consistent with differences in FCC matrix composition and phase connectivity arising from processing history.

Among the three conditions studied, 90CRA exhibits the highest coercivity values. At 2 K, H_c reaches 41.7 Oe, significantly higher than both SA750 and SA, indicating strong resistance to domain wall motion. This is attributed to effective pinning by rod-shaped $L1_2$ precipitates that form along grain boundaries during annealing. With increasing temperature, H_c decreases steadily to 28.8 Oe at 10 K, 23.8 Oe at 50 K, and 2.5 Oe at 100 K (Fig. 8b). H_c decreases steadily with

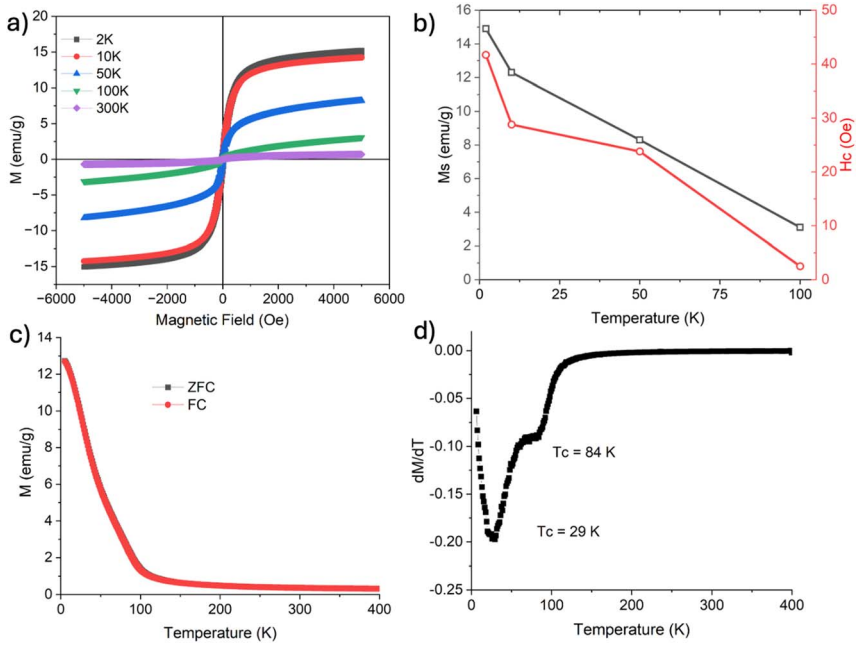

Fig. 8 Magnetic behaviour of the 90CRA condition. (a) *M*–*H* loops measured at 2, 10, 50, 100, and 300 K. (b) Temperature dependence of saturation magnetization (M_s) and coercivity (H_c), indicating a decrease in M_s and a decreasing trend in H_c with increasing temperature. (c) ZFC and FC magnetization curves recorded under a 1000 Oe field, showing a continuous decrease in magnetization with temperature. (d) d*M*/d*T* plot highlighting two magnetic transitions, with Curie temperatures identified at ~84 K and 29 K.

temperature, in contrast to the nonmonotonic trend observed in SA750. This behaviour is attributed to strong domain wall pinning by rod-shaped $L1_2$ precipitates, which becomes progressively less effective with increasing temperature.[23] The continuous decline in H_c across the two magnetic transitions (~29 K for $L1_2$ and ~84 K for the FCC matrix) reflects a gradual reduction in pinning strength and magnetic coupling in a more heterogeneous microstructural environment.

The magnetization *versus* temperature curves measured under ZFC and FC protocols in a 1000 Oe field reveal two magnetic transitions (Fig. 8c). The higher T_c around 84 K corresponds to the FCC matrix, while the lower transition near 29 K is attributed to magnetic ordering in the $L1_2$ precipitates (Fig. 8d). These precipitates, enriched in Al and Ti while retaining Ni and Co, become magnetically decoupled due to their size and boundary-localized distribution, giving rise to a distinct low temperature transition.

3.3.4. Room temperature magnetic behavior. The *M*–*H* loops measured at 300 K for all three conditions are shown in Fig. 9. Although the overall magnetization remains low, clear differences in coercivity are evident (inset of Fig. 9). The SA condition displays an almost linear response with negligible hysteresis, confirming its paramagnetic nature at room temperature. In contrast, both SA750 and 90CRA exhibit measurable coercivity, with 90CRA showing the largest

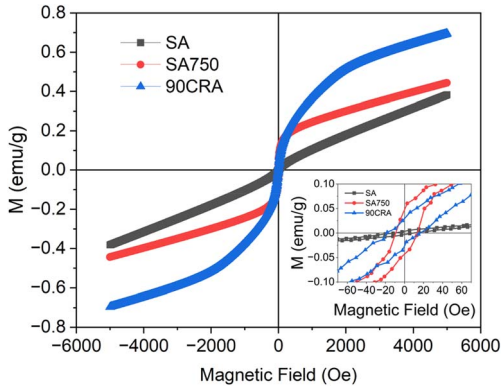

Fig. 9 Room temperature *M*–*H* loops for SA, SA750, and 90CRA. Full loops showing low magnetization across all conditions. (Inset) Zoomed-in view of the central region highlights negligible hysteresis in SA and finite coercivity in both SA750 and 90CRA.

hysteresis. The weak hysteresis in SA750, despite the absence of any identified secondary magnetic phase, may arise from residual short-range magnetic interactions or frozen magnetic clusters in the FCC or $L1_2$ phases. In 90CRA, however, the higher coercivity is consistent with the presence of a minor $L2_1$ Heusler-like phase at grain boundaries, previously identified by electron diffraction and EDS,[7,24] as well as possible discontinuities or magnetic inhomogeneities in the FCC matrix introduced by the rod-shaped precipitates.

4. Conclusion

The magnetic properties of the $Al_{0.2}Ti_{0.3}Co_{1.5}CrFeNi_{1.5}$ alloy were examined in three processing conditions: solution-annealed (SA), annealed at 750 °C (SA750), and cold-rolled plus annealed (90CRA). The SA condition exhibited a single magnetic transition near 48 K and low coercivity, consistent with a fully FCC matrix containing fine, coherent $L1_2$ precipitates. In SA750 and 90CRA, the growth and redistribution of the $L1_2$ phase led to magnetic decoupling, reflected in the emergence of two magnetic transitions and an increase in coercivity. The highest low temperature coercivity was observed in 90CRA, where rod-shaped $L1_2$ precipitates formed along grain boundaries. At 300 K, weak hysteresis was present in both SA750 and 90CRA. In the latter, this behaviour is attributed to a minor $L2_1$ Heusler-like phase located at grain boundaries. These results demonstrate that the magnetic response in this alloy system can be tuned through processing, by controlling phase morphology and chemical partitioning. More broadly, the findings highlight how nanoscale chemical ordering and microstructural architecture can be exploited to design magnetic materials with tailored coercivity and transition behaviour for cryogenic and multifunctional applications.

Data availability

The authors confirm that the raw data supporting the findings of this study are available from the corresponding author, upon reasonable request.

Conflicts of interest

There are no conflicts to declare.

Acknowledgements

The authors acknowledge financial support from the Åforsk Foundation, Sweden (Award ID 24-571), and from the Areas of Advance in Production, Materials, and Energy at Chalmers University of Technology. This work was also supported by the U.S. Air Force Office of Scientific Research under grant FA9550-17-1-0395, the National Research Foundation, Singapore, under its 29th Competitive Research Program (Award ID NRF-CRP29-2022-0002), and the AME Programmatic Fund by the Agency for Science, Technology and Research (A*STAR), Singapore (Grant No. A1898b0043).

References

1 B. Cantor, I. T. H. Chang, P. Knight and A. J. B. Vincent, Microstructural development in equiatomic multicomponent alloys, *Mater. Sci. Eng. A*, 2004, **375–377**, 213–218.
2 J.-W. Yeh, S.-K. Chen, S.-J. Lin, J.-Y. Gan, T.-S. Chin, T.-T. Shun, *et al.*, Nanostructured High-Entropy Alloys with Multiple Principal Elements: Novel Alloy Design Concepts and Outcomes, *Adv. Eng. Mater.*, 2004, **6**, 299–303.
3 D. B. Miracle and O. N. Senkov, A critical review of high entropy alloys and related concepts, *Acta Mater.*, 2017, **122**, 448–511.
4 E. P. George, D. Raabe and R. O. Ritchie, High-entropy alloys, *Nat. Rev. Mater.*, 2019, **4**, 515–534.
5 V. Chaudhary, R. Chaudhary, R. Banerjee and R. V. Ramanujan, Accelerated and conventional development of magnetic high entropy alloys, *Mater. Today*, 2021, **49**, 231–252.
6 W. H. Liu, T. Yang and C. T. Liu, Precipitation hardening in CoCrFeNi-based high entropy alloys, *Mater. Chem. Phys.*, 2018, **210**, 2–11.
7 S. Dasari, Y. J. Chang, A. Jagetia, V. Soni, A. Sharma, B. Gwalani, *et al.*, Discontinuous precipitation leading to nano-rod intermetallic precipitates in an $Al_{0.2}Ti_{0.3}Co_{1.5}CrFeNi_{1.5}$ high entropy alloy results in an excellent strength-ductility combination, *Mater. Sci. Eng. A*, 2021, **805**, 140551.
8 X. Xu, K. P. Davidson, L. P. Tan, S. Gorsse, V. Chaudhary and R. V. Ramanujan, Improvement in mechanical as well as magnetic properties of a $(FeCoNi)_{90}Ti_{10-x}Al_x$ complex concentrated alloy series by tuning the chemical order, *Scr. Mater.*, 2025, **254**, 116333.
9 A. Kovács, N. B. Venkataraman, V. Chaudhary, S. Dasari, T. Denneulin, R. V. Ramanujan, *et al.*, Role of heterophase interfaces on local coercivity mechanisms in the magnetic $Al_{0.3}CoFeNi$ complex concentrated alloy, *Acta Mater.*, 2023, **246**, 118672.
10 V. Chaudhary, M. S. K. K. Y. Nartu, S. Dasari, S. M. Varahabhatla, A. Sharma, M. Radhakrishnan, *et al.*, Magnetic and mechanical properties of additively manufactured $Al_x(CoFeNi)$ complex concentrated alloys, *Scr. Mater.*, 2023, **224**, 115149.

11 L. Han, Z. Rao, I. R. Souza Filho, F. Maccari, Y. Wei, G. Wu, *et al.*, Ultrastrong and Ductile Soft Magnetic High-Entropy Alloys via Coherent Ordered Nanoprecipitates, *Adv. Mater.*, 2021, **33**, 2102139.
12 L. Han, F. Maccari, I. R. Souza Filho, N. J. Peter, Y. Wei, B. Gault, *et al.*, A mechanically strong and ductile soft magnet with extremely low coercivity, *Nature*, 2022, **608**, 310–316.
13 S. Dasari, V. Chaudhary, B. Gwalani, A. Jagetia, V. Soni, S. Gorsse, *et al.*, Highly tunable magnetic and mechanical properties in an $Al_{0.3}$CoFeNi complex concentrated alloy, *Materialia*, 2020, **12**, 100755.
14 V. Chaudhary, R. Nirmala and Y. Huang, Magnetic materials and devices, *Mater. Res. Express*, 2025, **12**, 010201.
15 W. H. Teh, L. P. Tan, S. Chen, F. Wei, J. J. Lee, S. P. Padhy, *et al.*, Breaking conventional limits of silicon content in Fe-xSi magnetic alloys through additive manufacturing, *J. Alloys Compd.*, 2024, **983**, 173829.
16 V. Chaudhary, V. Soni, B. Gwalani, R. V. Ramanujan and R. Banerjee, Influence of non-magnetic Cu on enhancing the low temperature magnetic properties and Curie temperature of FeCoNiCrCu(x) high entropy alloys, *Scr. Mater.*, 2020, **182**, 99–103.
17 Z.-Z. Zhou, L.-J. Xu, Y.-T. Liu, L.-J. Hao, Y.-H. Zhang, R. Luo, *et al.*, Magnetic Shield Design and Simulation Optimization of Metallic Magnetic Calorimeter in Ultra-Low Temperature Working State, *J. Low Temp. Phys.*, 2024, **215**, 46–63.
18 M. Pelliccione, A. Jenkins, P. Ovartchaiyapong, C. Reetz, E. Emmanouilidou, N. Ni, *et al.*, Scanned probe imaging of nanoscale magnetism at cryogenic temperatures with a single-spin quantum sensor, *Nat. Nanotechnol.*, 2016, **11**, 700–705.
19 D. B. Williams and E. P. Butler, Grain boundary discontinuous precipitation reactions, *Int. Met. Rev.*, 1981, **26**, 153–183.
20 I. Manna, S. K. Pabi and W. Gust, Discontinuous reactions in solids, *Int. Mater. Rev.*, 2001, **46**, 53–91.
21 S. Dasari, A. Jagetia, A. Sharma, M. S. K. K. Y. Nartu, V. Soni, B. Gwalani, *et al.*, Tuning the degree of chemical ordering in the solid solution of a complex concentrated alloy and its impact on mechanical properties, *Acta Mater.*, 2021, **212**, 116938.
22 I. Škorvánek and R. C. O'Handley, Fine-particle magnetism in nanocrystalline Fe-Cu-Nb-Si-B at elevated temperatures, *J. Magn. Magn. Mater.*, 1995, **140–144**, 467–468.
23 G. Herzer, Modern soft magnets: Amorphous and nanocrystalline materials, *Acta Mater.*, 2013, **61**, 718–734.
24 S. Ghosh, S. Sangwan, S. Mandal, S. Datta, M. Kar, P. Singh, *et al.*, Room temperature giant magneto-caloric effect in $Ni_{45}Mn_{44}Sn_{11-X}In_X$ (X = 1, 3) disordered Heusler alloy: The role of martensite transition, *J. Magn. Magn. Mater.*, 2022, **562**, 169797.